Modeling CMAQ dry deposition treatment over Western Pacific: A distinct characteristic of mineral dust and anthropogenic aerosol

Steven Soon-Kai Kong[1], Joshua S. Fu[2], Neng-Huei Lin[1, 3, *], Guey-Rong Sheu[1, 3, *], Wei-Syun Huang[1]

[1] Department of Atmospheric Sciences, National Central University, Taoyuan, 32001, Taiwan
[2] Department of Civil and Environmental Engineering, the University of Tennessee Knoxville, TN37996, USA
[3] Center for Environmental Monitoring and Technology, National Central University, Taoyuan, 32001, Taiwan

Correspondence to: Neng-Huei Lin (nhlin@cc.ncu.edu.tw) and Guey-Rong Sheu (grsheu@atm.ncu.edu.tw)

Abstract. Dry deposition plays a vital role in the aerosol removal process from the atmosphere. However, the chemical transport model (CTM) is sensitive to the dry deposition parameterization and yet remains to be determined due to the limited particle deposition measurement. By utilizing the CMAQv5.4 with the refined dust emission treatment, the East Asian dust (EAD) simulation during January 2023 was constructed to evaluate the performance of four dry deposition parameterizations, namely PR11, E20, S22, and P22. The result showed that the dry deposition parameterization could significantly improve the CMAQ dust emission treatment. By implementing the E20 dry deposition scheme, the CMAQ simulation performance of the surface PM_{10} has been considerably improved with the NMB of -41.9 %, as compared to the dry deposition proposed by PR11 (54.05 %), S22 (-47.01 %) and P22 (-53.90 %). The modeled PM_{10} pattern by E20 at the upper level (700 hPa) was mostly consistent with the observed PM_{10} at the Lulin Atmospheric Background Station (LABS; 23.47° N, 120.87° E; 2862 m a.s.l.) where is a typical background site at Western Pacific, particularly in capturing the peak value. The high-altitude correlations (R) were well performed for E20 by 0.55, as compared to PR11 (0.47), S22 (0.54) and P22 (0.46). Moreover, E20 improved the simulated PM_{10} concentrations and aerosol optical depth (AOD) value over the Asian Continental during the multiple dust episodes in spring 2021. The noticeable deduction of the coarse mode particle's deposition velocity (V_d) was responsible for reducing the PM_{10} simulation underestimation. Moreover, the significant improvement of the modeled PM_{10} was also shown by the $PM_{2.5}$ simulation. On 22-31 January 2023, the *in-situ* measurement of the upper level observed the possibility of natural dust and anthropogenic aerosol. This is consistent with the CMAQ, which shows

that both aerosol types displayed a clear "long dust-black carbon belt" along the 15°N. We proposed implementing the E20 dry deposition approach, narrowing the uncertainty of the CMAQ dust emission treatment.

1 Introduction

The chemical transport model (CTM) is a powerful tool for comprehending air pollution, encompassing emission, transport, radiative impact, and removal mechanisms at various grid scales. Among these, particle dry deposition is a crucial aerosol removal process and an important sink for particles in the model. The derivation of the dry deposition is based on the resistance framework and electrical analogue, but its implementation can vary across models (Wesley, 1989; Giardina and Buffa, 2018; Gaydos et al., 2007; Khan and Perlinger, 2017; Shu et al., 2017). A key challenge in dry deposition simulation is the scarcity of measurement data for model verification, underscoring the necessity for further research to enhance the accuracy of air quality modeling.

An immense range of dry deposition parameterization has been implanted in the model. The deposition mechanism by Slinn (1982) includes the deposition process such as turbulent transfer, Brownian diffusion, impaction, interception, gravitational settling, and particle rebound, where the particle grows under humid conditions. Zhang et al. (2001) suggested the dry deposition scheme is sensitive to land use category and several parameters. For instance, due to the particle growth, the deposition velocity (V_d) over the ocean is much higher than on another land surface, as the V_d increased rapidly with the increase of particle size. However, Zhang et al. (2001) parameterization still underestimated the global $PM_{2.5}$ concentration. The latest dry deposition scheme revision by Emerson et al. (2020) has reduced the uncertainty, marking a significant step forward in our quest for more accurate air quality modeling.

An updated deposition scheme that reduces the dependence of the deposition velocity on the aerosol mode width has been proposed (Shu et al., 2022). Indeed, the approach suggested that vegetation dependence increased the V_d for submicrons and decreased for large particles by 37 % and -66 %, respectively. It also reduced the functional biases by 56-97 % for vegetated land-use type and equivalence performance over the water. Moreover, adding the second inertial impaction term for microscale obstacles such as leaf hairs, microscale ridges, and needle leaf edge effects managed to increase the mass dry deposition of the accumulation mode aerosols in the model (Pleim et al., 2022). These modifications reduced the average PM2.5 in the atmosphere during July 2018 over the contiguous United States.

With a plethora of deposition approaches in use, it becomes paramount to comprehend their impact on model performance in predicting aerosol behavior. The surface fine particle concentrations can vary up to 5-15 %, and the particle dry deposition has more than 200 % discrepancy due to the different dry deposition schemes. (Saylor et al., 2019). A comprehensive evaluation of five different parameterizations has been conducted, with the simplest and most effective deposition mechanism suggested for the CTM (Khan and Perlinger, 2017). However, the model's reliance on meteorological factors such as frictional velocity, relative humidity, rainfall, or wind speed, which can significantly influence the model's accuracy, remains a challenge (Kong et al., 2021).

Besides the model bias on $PM_{2.5}$, the simulation of PM_{10} has been underestimated due to the uncertainty of the deposition mechanism, particularly over the western Pacific (Kong et al., 2021). The V_d is overestimated for coarse particles, where the dry deposition velocity is too high for coarse particles when the frictional velocity is large, which is why the surface PM_{10} concentration is underestimated (Ryu and Min, 2022). The model performance of PM_{10} simulation that is widely influenced by the dust treatment embedded within CMAQ has been revised (Dong et al., 2016; Liu et al., 2021; Kong et al., 2021, 2024) and are found to effectively simulate the PM_{10} over the western Pacific region such as Taiwan. However, the issue regarding the deposition algorithm's impact on the model performance at the corresponding region needs to be discussed. The present research intends to evaluate the CMAQ model performance due to the different deposition schemes on aerosols in the Taiwan region.

The model performance in Taiwan is paramount in our study, as the area is equipped with a substantial number of well-maintained surface observation sites, providing comprehensive coverage. The LABS station in the high-altitude subtropical western North Pacific region serves as the sole background station for monitoring transboundary pollutants. This station is crucial in our research as it provides unique data on the long-range transport of pollutants, further underscoring the relevance of our study.

The transboundary pollutants mechanisms have been widely discussed through LABS measurements, cooperating with the backward trajectory, reanalysis dataset, and modeling approach. Previous research reveals that LABS pollutants could be associated with severe fire emissions from northern Peninsular Southeast Asia (Huang et al., 2020; Ooi et al., 2021) and Indonesia (Ravindra Babu et al., 2023). Moreover, the intense wind speed in northwest China could transport the mineral dust through the surface and high-altitude layer detected at LABS (Kong et al., 2021; Kong et al., 2022). Additionally, the transport process of East Asian haze due to the cold surge from the Asian Continental industrial region towards Taiwan has been widely discussed (Chuang et al., 2020). Instead of pure aerosol, the coexistence of dust and biomass burning over Taiwan, a condition discovered in previous research, has significant implications for the regional climate (Dong et al., 2018; Dong et al., 2019). However, the high-altitude synoptic pattern associated with the coexistence between natural dust and anthropogenic pollutants remains unknown due to a lack of observations at the upper layers.

This study used the chemical transport model to investigate the long-range transport of East Asian dust (EAD) that occurred on 22-31 January 2023 and 12 March-20 April 2021. Due to the limitation of the dust model, the CMAQ version 5.4, embedded with four types of dry deposition schemes, was implemented to justify the effectiveness of improving our latest refined dust model (Kong et al., 2024). LABS detected the recent transboundary episode in January 2023 as a mixing aerosol type (see Section 3.1), which has not been widely discussed, and the multiple dust storm episodes mentioned by Kong et al. (2024) provide an opportunity to model the EAD over the downwind region. Recognizing the significant transboundary events detected through Taiwan's observations, the improvement of the CMAQ dust model by the dry deposition schemes, and its application in characterizing the transport mechanism can be vital. The paper is organized as follows. The model setup and ancillary datasets are discussed in Sect. 2. The results and discussion are presented in Sect. 3, followed by the conclusions in Sect. 4.

2 Data and Methodology

2.1 Dust emission treatment

Before delving into the details, it's important to understand the process of dust transport. Dust is primarily transported by wind through a process known as sandblasting (Kok et al., 2012). For dust to be uplifted, the horizontal wind speed must exceed a certain threshold frictional velocity ($u_{*,t}$), which is estimated by the model as follows:

$$u_{*,t} = u_{*,to} f_m f_r \tag{1}$$

Where $u_{*,to}$ is the ideal threshold friction velocity, while f_m and f_r are the correction factors of soil moisture and surface roughness, respectively.

Through a collaborative effort, the windspeed, soil texture, soil moisture, and surface roughness length derived from field and laboratory studies have been integrated into the windblown dust treatment, which is now a part of the Community Multiscale Air Quality (CMAQ) modeling system (Foroutan et al., 2017). This model, developed and evaluated over the continental United States, has also been extended to the East Asia region (Dong et al., 2016; Liu et al., 2021; Kong et al., 2021, 2024). Kong et al. (2024) have proposed further improvements, including the integration of the revised soil moisture fraction, dust emission speciation profile, and bulk soil density, to enhance the representation of the Asian dust simulation. This ongoing collaboration is crucial for the continuous improvement of our understanding and management of dust emissions.

2.2 Particle dry deposition schemes

Particle dry deposition is a complex process relating to the deposition velocity, particle size, source and composition, land use surface, and meteorological condition. Generally, the flux of the particle mass through the surface boundary layer is estimated as:

$$F = C \times V_d \tag{2}$$

where F is the deposition flux, C is the particle concentration at the surface layer, and V_d is the deposition velocity.

The difference in the particle concentration and deposition prediction among the various atmospheric chemistry models was probably due to the algorithm of the dry deposition particle. The algorithm describing particle deposition velocity as a function of particle size in almost all current air quality model systems is descended from Slinn (1982). The particle deposition according to vegetative canopies formulated the deposition velocity as:

$$V_d = V_s + \frac{1}{R_a + R_s} \tag{3}$$

where V_s is the gravitation settling velocity, R_a is the resistivity aerodynamic and R_s is the surface resistivity. The V_s is calculated according to Stokes's Law as:

$$V_s = \frac{p_p\, D_p^2\, g C_c}{18\eta} \tag{4}$$

where, p_p is the density of the particle; D_p is the diameter of the particle; g is gravitational acceleration; C_c is the Cunningham correction factor for small particles; and, η is the dynamic viscosity of air.

CMAQ is embedded with M3Dry dry deposition calculation that implements the scheme of Pleim and Ran (2011), which is based on Slinn (1982). As noted by Pleim and Ran (2011), chemical surface flux modeling has become an essential process in the air quality model. For instance, the linkages of ambient concentration levels to the deposition of SO_x and NO_x. Moreover, Surface Tiled Aerosol and Gaseous Exchange (STAGE) deposition has been implemented within the CMAQv5.3, where estimated fluxes from sub-grid cell fractional land-use values, aggregate the fluxes to the model grid cell and unifies the bidirectional and unidirectional deposition schemes using the resistance framework (Massad et al., 2010; Nemitz et al., 2001). The updated STAGE version in CMAQv5.4 could aggregate the grid-scale values that match the grid-scale values from most kinds of Land Surface Model of WRF (Hogrefe et al., 2023).

2.3 CMAQ model design

This study applied WRF v4.0 for the meteorological field parameters and CMAQv5.4 to simulate the transboundary East Asian dust episodes on 22-31 January 2023, and the multiple dust storm episodes during 12 March-20 April 2021. The modeling domain was set up to cover the Taklamakan and Gobi Desert, with a resolution of 45 km, and nested towards Taiwan at a resolution of 15 km (d02) and 5 km (d03) (Fig .1, Table 2). Also, as Taiwan is influenced by biomass burning, the domain covers up to the peninsular Southeast Asia (PSEA), which will be carried out in the future (Ooi et al., 2021). The model consisted of 40 vertical layers, with eight layers below~1 KM altitude, 13 layers below ~3 KM altitude, and 27 layers covering the upper layer to ~21 KM. The model's initial and lateral boundary conditions were constructed using the National Centers for Environmental Prediction (NCEP) Final Analyses (FNL) reanalysis dataset on a 0.5◦ ×0.5◦ grid. The data assimilation was conducted by grid nudging in all the domains. The CB06 gas-phase chemical mechanism and the AERO7 aerosol module model were implemented in CMAQ for the present study.

The anthropogenic emission inventories in East Asia, crucial for our research, were obtained from the MICS-Asia (Model Inter-Comparison Study for Asia) Phase III emission inventory (Li et al., 2017). The emissions of SO_2, NOx, NMVOC, NH_3, CO, PM_{10}, $PM_{2.5}$, BC, OC and CO_2 has been meticulously modified, taking into account of the relative changes in China's anthropogenic emissions between 2010 and 2017 (Zheng et al., 2018). Additionally, the modified emission of NO_2 was adjusted further by the satellite imagery OMI-NO_2 in January 2023 (Huang et al., 2021). Biogenic emissions for Taiwan were prepared by the Biogenic Emission Inventory System version 3.09 (BEIS3, Vukovich and Pierce, 2002) and, for regions outside Taiwan, by the Model of Emissions of Gases and Aerosols from Nature v2.1 (MEGAN, Guenther et al., 2012). TEDS 10.0 (Taiwan Emission Database System, TWEPA, 2011; https://erdb.epa.gov.tw/,last access: 18 January 2024) was used for domain 3 (d03).

To ensure the precision of the multiple dry deposition parameterizations, the present research conducted six simulation scenarios, namely CMAQ_Off_PR11, CMAQ_Dust_PR11, CMAQ_Dust_E20, CMAQ_Dust_S22 and CMAQ_Dust_P22. The CMAQ_Off_PR11 scenario did not include the inline dust calculation (Table 2). Meanwhile, the latest refined integrated dust treatment was implemented in the CMAQ_Dust_PR11 scenario (Kong et al., 2024). Indeed, both CMAQ_Off_PR11 and CMAQ_Dust_PR11 used the dry deposition mechanism by Pleim and Ran (2011). The dry deposition mechanism of Emerson et al. (2020), Shu et al. (2022), and Pleim et al. (2022) were implemented in CMAQ_Dust_E20, CMAQ_Dust_S22, and CMAQ_Dust_P22 scenarios, respectively.

2.4 Ancillary dataset

PM_{10} (particulate matter ≤10 μm in aerodynamic diameter) and $PM_{2.5}$ (particulate matter ≤2.5 μm in aerodynamic diameter) concentrations during the dust events in January 2023 were obtained from Lulin Atmospheric Background Station (LABS; 23.47° N, 120.87° E, 2862 m MSL) and Cape Fuguei (25.30° N, 121.54° E, 10 m MSL). In addition, the hourly PM_{10} and $PM_{2.5}$ of nearly 100 sites distributed over mainland China (Fig. S1), covering the period of 12 March-20 April 2021, obtained from the Chinese air quality online monitoring analysis platform's website (www.aqistudy.cn/). The Modern Era Retrospective-analysis for Research and Application version 2 (MERRA-2) reanalysis data was used to demonstrate the spatiotemporal distribution of dust, compare with the air quality model, irrespective of the influence of clouds. MERRA-2 (Gelaro et al., 2017) is a NASA reanalysis utilizing Goddard Earth Observing System Data Assimilation System Version 5 (GEOS-5) and covering the data assimilated system at a native spatial resolution of 0.5 ∘ × 0.625 ∘. Also, Moderate Resolution Imaging Spectroradiometer (MODIS) Terra satellite images and the level-3 MODIS AOD at 550 nm (MYD08) were obtained from the U.S. National Aeronautics and Space Administration (https://worldview.earthdata.nasa.gov/).

3 Results and Discussion

3.1 Observed air quality and weather conditions

Figure 2 shows the dust outbreak over East Asia, displayed by the MODIS Terra sensor and MODIS AOD at 550 nm from 22-31 January 2023. The satellite image showed dust induced by a high-pressure system on 24-25 January (Fig. 2a3, 2a4). The next day, the same region was covered by a thick cloud, and dust was again widely distributed from 27-30 January 2023. Using MODIS AOD to verify the dust plume (Han et al., 2012; Kong et al., 2021), the dust plume was distributed in Central China and northern Taiwan on 24 January 2023. Moreover, the most intense dust plume in the eastern China and East China Sea region was observed on 27 January. Fig. S2 shows the synoptic weather map across the study domain.

On 22-23 January, the southward high-pressure system was responsible for pushing the pollutant across the Asian Continent, which is consistent with Chuang et al. (2018) and Kong et al. (2021, 2022, 2024) (Fig. S1a-b). The high-pressure system that moved southward will then move eastward toward the western Pacific Ocean (Fig S1c-d). Meanwhile, the high-pressure system on the northwest side again expands in the southeast direction. The second high-pressure system again pushed the pollutant for the second time and caused the high pollutant problem on 27 January.

The impact of East Asian dust on the air quality over the high-altitude western Pacific region was widely discussed (Kong et al., 2022). Two interesting high pollution events at Mt. Lulin (2,862 m above sea level) during 24-26 Jan and 27-30 January, respectively, are shown in Fig. 3. The latter event was more intense compared to the earlier one, where the maximum PM_{10} concentration can reach up to 35 μg m^{-3}. Moreover, it was observed that the black carbon concentrations could reach up to a maximum of 400 ng m^{-3}. Based on the *in-situ* measurement, it was interesting to find the mixing state between dust, black carbon, and brown carbon (Fig. 3c). Different from what has been discussed by Kong et al. (2022), the long-range transport air pollution at the high-altitude not just merely EAD, but also included the anthropogenic pollutant from mainland China.

3.2 Evaluation of CMAQ dust emission and dry deposition parameterizations

Table 3 shows the statistical analysis of PM_{10} and $PM_{2.5}$ concentrations over Cape Fuguei (northern Taiwan) from 22-31 January under the multiple deposition mechanisms. The threshold of the statistical index is based on Emery (2001). CMAQ_Off_PR11, the PM_{10} simulation presented without the inline dust calculation, recorded the normalized mean bias (NMB) of -57.59 %. CMAQ_Dust_PR11 improved the simulation over Cape Fuguei (northern Taiwan) by -54.05 % as we included the refined dust treatment (Kong et al., 2024). However, the improvement is insignificant due to the weak intensity dust episodes and the limitation due to the excessive deposition mechanism within the model (Kong et al., 2021). Hence, we expanded the sensitivity simulation to examine the impact of the deposition algorithm on the aerosol prediction. CMAQ_Dust_E20 simulations utilizing the Emerson et al. (2020) approach increased the modeled PM_{10} simulation by NMB of -41.9 %. In addition, the deposition algorithm proposed by

CMAQ_Dust_S22 (Shu et al., 2022) and CMAQ_Dust_P22 (Pleim et al., 2020) has reduced the NMB by -47.01 % and -53.90 %, respectively.

Instead of PM_{10} simulation, the present study found that the inline dust treatment and deposition algorithms could influence $PM_{2.5}$ simulation performances. For instance, the modeled $PM_{2.5}$ improved from -19.55 % (CMAQ_Off_PR11) to -16.53 % (CMAQ_Dust_PR11). Meanwhile, the deposition algorithm embedded in CMAQv5.4 has further enhanced the modeled $PM_{2.5}$ by -10.65 %, -15.22 %, and -8.84 % under CMAQ_Dust_E20, CMAQ_Dust_S22 and CMAQ_Dust_P22, respectively. This incident suggested that the East Asian dust from northwest China transported to the Western Pacific Ocean could also carry the anthropogenic emission of East China.

Figure 4 shows the time series of hourly PM_{10} and $PM_{2.5}$ concentrations over Cape Fuguei (northern Taiwan) and LABS (high altitude region) from 22-31 January 2023 under the multiple deposition mechanisms. Generally, all the patterns of PM_{10} simulations were consistent with the observed PM_{10}, especially in capturing the peak value. For instance, the maximum observed (CMAQ_Dust_E20) PM_{10} concentrations at the surface during Jan 24 and 27 were 141 (102.6) μg m^{-3} and 114 (163.2) μg m^{-3}, respectively. A similar time-series pattern was found for the $PM_{2.5}$ simulation (Fig. 4b).

More importantly, the CMAQ model performance over the high-altitude region needed to be carried out and discussed. The biomass-burning episode of the northern PSEA over Mt. Lulin has been finely correlated by plume rise injection (Chuang et al., 2016; Ooi et al., 2021). From Fig. 4c, the modeled PM_{10} pattern for CMAQ_Dust_Off could not correlate well with observed PM_{10} over Mt. Lulin, with a poor correlation of 0.17. The correlation was increased for CMAQ_Dust_PRll (0.47), CMAQ_Dust_S22 (0.54), CMAQ_Dust_P22 (0.46), and primarily well performed for CMAQ_Dust_E20 (0.55). The modeled result was somehow consistent with the surface PM_{10} simulation at Cape Fuguei. The high observed PM_{10} episodes during 27-28 January with a maximum of 34.5 μg m^{-3} was only 53.3 % higher than CMAQ_Dust_E20 of 22.5 μg m^{-3}. For the CMAQ $PM_{2.5}$, the simulation generally underestimated the observed $PM_{2.5}$.

During the spring of 2021, a series of dust storms (15 March, 27 March, and 18 April) occurred over the Gobi area, with one of the most significant dust storms in the past decade (15 March, the “3.15” dust storm hereafter) causing environmental impact over the continental (Jin et al., 2022; Gui et al., 2022; He et al., 2022; Liang et al., 2022; Tang et al., 2022). More interestingly, one of the multiple dust storm episodes reached western Pacific Ocean due to the extreme typhoon episode (Kong et al., 2024). Hence, we intend to re-emphasize the precision of various deposition schemes on the CMAQ for the recent dust storm episode over the Asian Continental highlighted by Kong et al. (2024). We evaluated the CMAQ simulations with the different dry deposition schemes for the 40-day sensitivity test on 12 March-20 April 2021 against measured PM_{10} and $PM_{2.5}$ concentrations across the observation sites in mainland China (Table 4). The observation sites used for the model comparison are marked in Fig. S1. Generally, the evaluation results for Taiwan and mainland China were consistent. During the 40 days of Spring 2021, the CMAQ PM_{10} of NMB was the highest for Off_PR11 (NMB = -79.19 %), followed by Dust_PR11 (-60.53 %). The latest inline dust emission scheme embedded with E20 dry deposition scheme for PM_{10} was well performed by NMB of -25.43 %, compared to the Dust_S22 (-45.97 %) and Dust_P22 (-59.82 %). For the $PM_{2.5}$ simulation, Dust_PR11 has been improved from Dust_Off, and Dust_S22 was slightly better than Dust_E20.

Figure 5 shows the scatter plot of simulated and observed PM across mainland China. The correlation coefficient (R), a factor of two (FAC2), and the mean observed and simulated PM are marked in Figure 5. The modeled PM_{10} without the dust scheme had the lowest correlation, followed by Dust_PR11. Among all of these simulations, Dust_E20 performed the best correlation ($R > 0.3$) compared to Dust_PR11, Dust_S22 and Dust_P22. However, for $PM_{2.5}$, the correlation between the model and measured values was similar for all the dry deposition schemes. The statistical index of FAC2 was used in the present work since either low or high outliers less influence it (Chan and Hanna, 2004). The dataset is reliable for FAC2 values between 0.5 and 2.0, with the ideal model of 1.0. The simulated PM_{10} by E20 performed well, with a nearly perfect value of 1.1. Meanwhile, the $PM_{2.5}$ by S22 simulation was slightly better than E20 but much better than the other experiments.

The comparison of AOD between CMAQ and MODIS for the three dust storm episodes: 14-16 March 2021 ("3.15" dust storm), 26-28 March 2021 2021 ("3.27" dust storm), and 17-19 April 2021 was shown ("4.18" dust storm) (Table 4). Overall, CMAQ Dust_E20 above 30°N has evaluated well the MODIS AOD by NMB of -26.2 %, as compared to PR11 (-37.4 %), S22 (-32.0 %) and P22 (-35.8 %). The CMAQ AOD by E20 during the most intense Super Dust Storm in 3.15 has significantly improved over northern China, the dust source region, as shown in the red dash rectangular box (Fig. S3). Additionally, the modeled AOD by E20 over the western Pacific Ocean (shown in red dash rectangular box) increased in episode 4.18, reporting a value of 0.7 compared to 0.4 by PR11. Significantly, the E20 deposition scheme has primarily enhanced the PM_{10} prediction over the marine boundary layer, addressing the model uncertainty due to the typhoon mentioned by Kong et al. (2024) and demonstrating the practical implications of our research.

The present work is consistent with the dust scheme in the WRF-Chem, where the dust loading is very sensitive to the dry deposition schemes and dust emission schemes, especially over the downwind region (Zeng et al., 2020). Fig. 6 shows the CMAQ estimated ten days averaged mean PM_{10} and $PM_{2.5}$ for the PR11 deposition scheme and its corresponding change by E20, S22, and P22, respectively. Generally, the spatial distribution of the high PM_{10} concentrations by > 80 μg m^{-3} was distributed over northwest China, which is the dust source region's location, consistent with the simulation suggested by Kong et al. (2021, 2022, 2024). Such high particulate matter dissipated to east China, indicating the transport pathway in the southeastern direction towards the western Pacific (Fig. 6a). The difference between E20 and PR11 suggested the high PM_{10} > 50 μg m^{-3} distributed over northwest China, meaning E20 successfully increased the PM_{10} concentrations. As compared to the S22 deposition scheme, it also increased the PM_{10} over northwest China by around 30 μg m^{-3} but was not as intense as E20. For P22, the difference of PM_{10} between PR11 and P22 was less than 10 μg m^{-3}, indicating less efficiency of P22 in improving the PM_{10}. Another fascinating fact about E20 was that the PM_{10} increased over the southern South China Sea. For the modeled $PM_{2.5}$ concentrations, the high concentration was distributed over the Asian Continental. Under the E20 mechanism, the modeled $PM_{2.5}$ has been increased over PSEA. For S22, such improvement of $PM_{2.5}$ was more intense over a similar region.

Meanwhile, the $PM_{2.5}$ simulated by P22 didn't have much difference compared to PR11, which showed consistency as the PM_{10} simulation.

3.3 Impact on the CMAQ ambient particle concentrations

Figure 7 shows the boxplot of the 10-day averaged simulated V_d for the Aitken, accumulation, and coarse particles modes under multiple deposition schemes, namely PR11 (Pleim and Ran, 2011), E20 (Emerson et al., 2020), S22 (Shu et al., 2022) and P22 (Pleim et al., 2022). Different dry deposition treatments substantially impact aerosol profile, altering the ambient total dry deposition regionally. As shown in the figure, the median of E20, S22, and P22 increased the deposition velocity of the Aitken (accumulation) modes particle as compared to PR11 by 22.56 (11.32) %, 117.76 (86.43) % and 2.5 (7.52) % respectively. For coarse-mode particles, the P22 simulation median V_d increased by 14.36 % compared to PR11. On the other hand, E20 and S22 showed a different simulation by the median V_d reduction by -9.1 % and -12.1 %, respectively. Also, the 75th percentile V_d of the coarse mode has been significantly reduced by -50.57 % (E20) and -58.27 % (S22), respectively. The result suggested that the reduced V_d of the coarse mode particle was responsible for reducing the PM_{10} simulation underestimation of PR11, consistent with the simulation by Shu et al. (2022) and Ryu and Min (2022). The slow V_d means the total loss of aerosol to the surface has been minimized, leading to increased aerosol concentration.

We estimated the CMAQ averaged particle modes for the PR11 dry deposition scheme and the corresponding percentage changes using E20, S22, and P22 (Fig. 8 and Fig. S4). By using E20 and S22, we found that the V_d corresponding to the Aitken and accumulation modes has been increased by >100 % over most of the CMAQ domain, which was most obvious over Asian continent (Fig 8b, c, f, g). Meanwhile, the variation of V_d distribution was insignificant for P22 (Fig. 8d, h, i). For the coarse mode particles, the V_d has been tremendously reduced for E20 and S22 compared to PR11. However, for S22, the V_d has increased by >100 % over northwest China, which is the dust source region (Fig. 8k). This leads to a significant deposition over the desert before transporting it to the downwind region, causing less PM_{10} simulated by S22 than E20. A previous study proposed the V_d for the aerosol at the water surface was associated with the CTM uncertainly at the downwind region (Kong et al., 2021, 2024; Ryu and Min, 2022). The V_d of Aitken and accumulation modes at land and water surfaces increased generally, except E20 at the water surface. Interestingly, the coarse mode V_d at the water surface for E20 and S22 decreased significantly by -44.65 % and -21.44 %, respectively, suggesting that both deposition schemes, particularly E20, could resolve the excessive deposition over the marine boundary layer (Table 5). Such minimal deposition velocity distributing over a large part of the western Pacific Ocean, including the Sea of Japan, Yellow Sea, East China Sea, and South China Sea, might be responsible for reducing the modeled PM_{10} underestimation over Taiwan (Fig.8j, k), as mentioned by Kong et al. (2021).

3.4 CMAQ of dust and black carbon synoptic pattern at the upper level

Black carbon, often known as elemental carbon, released from the biofuels, fossil fuels and biomass burning, has been proven to impact the radiative budget and regional climate (Ramanthan, V and Carmicheal, 2008; Pani et al., 2016, 2020). In the meantime, China has been a significant contributor to global anthropogenic black carbon emission, particularly in the cities of the northern part (Xiao et al., 2023; Wang et al., 2024). During the severe dust episodes in the spring of 2023, the contribution of black carbon brought by EAD was captured in North China (Wang et al., 2024). As depicted in Fig. 2, the transboundary episode observed in the upper level of Taiwan during this event could be the mixing of the natural dust and anthropogenic haze episodes, which demonstrates the consistency. Additionally, blending mineral dust with anthropogenic transport due to the north easterly wind, a wind that blows from the northeast, has been a subject of extensive discussion (Lin et al., 2007, 2012; Li et al., 2012). During the EAD, the dust from the Gobi Desert that was transported towards the western Pacific region could also carry anthropogenic aerosol, contributing to different levels of pollutant concentration. However, the distinct transport pathway at the high altitude between both aerosol types is a topic that has received less attention but is of significant importance to our understanding of atmospheric dynamics.

Figure 9 illustrates mineral dust concentration's spatial and temporal distribution under the CMAQ_Dust_E20 scenario at 700 hPa from 24-30 January. The model reveals a high proportion of modeled dust aerosol (red dash circle) at the source region, indicating an uplift from the surface to 700 hPa (Fig. 9a, b). This uplift, driven by the strong pressure gradient at the surface and the 'eastward moving trough system' at the upper level (700 hPa), is a key factor in the eastward and southward transfer of the dust (Fig. 9c, d). The high dust fraction reappears at the source region (Fig. 9e-f) and is transported eastwardly by the similar upper-level trough (Fig. 9g-j), causing a long dust belt at 15°N, distributing over central Asia continental, Taiwan Straits, Taiwan and large part of western Pacific Ocean. (Fig. 9i, j). On 29 January, the model of E20 clearly predicted that the dust plume moved in the southward direction toward the South China Sea (Fig. 9k, l). The dust aerosol was left distributed at a certain part of the northern South China Sea and the Philippine Sea until it totally dissipated (Fig. 9m, n). This interesting result suggests the possible EAD at the longer distance at the upper level, which is a topic for further investigation.

The southward high-pressure system responsible for the long-range transport haze episode has been widely discussed (Chuang et al., 2008; Kong et al., 2021)—however, the upper-level transboundary transport needs to be addressed more. While focusing on CMAQ_Dust_E20, we attempted to characterize the long-range transport of modeled black carbon at the upper level (700 hPa) (Fig. 10). As shown in Fig. 10(c, e), the modeled black carbon concentration is shown to be significantly distributed at central China. The black carbon transport pattern followed the eastward-moving trough system as the plume moved eastward and southward (Fig. 10g-l). Interestingly, the long black carbon belt is consistent with the long dust belt, as shown in Fig. 9. For instance, both modeled dust and black carbon were distributed at the western Pacific Ocean (Fig. 9i, j; Fig. 10i, j) and South China Sea (Fig. 9m, n; Fig 10m, n). This means that the black carbon due to the anthropogenic emission and the natural EAD shared a similar transport pattern at the upper level, driven by the trough system. Such consistency has been verified by the MERRA-2 dust and black carbon mass column over the region (red dash rectangular in Fig. S5).

Dust aerosol vertical profiles (Fig. 11) show the large dust fraction was distributed over the Asian Continent (Fig. 11a, b), according to the transect drawn as a red-dash line in Fig. 1. Due to the westerly winds as illustrated in Fig. 9, the aerosol plume transported at the eastward direction toward the western Pacific Ocean, that vastly accumulated along the 700 hPa altitude. Another plume was found across the ocean on the east side of Taiwan Island (Fig. 11b). The plume was moved eastward (Fig. 11c-f). During 00 UTC on 27 January, another large fraction of dust covered the Asian Continent (Fig. 11g); in the next 12 hours, the model showed an apparent dust plume located in the Western Pacific Ocean, with much higher dust concentrations compared to Fig. 11b. The plume again distributed eastward showed a clear dust dome (Fig. 11i-j). Then, due to the westerly airflow, the dust aerosol slowly dissipated at the upper layer of the western Pacific.

The vertical profile of the modeled black carbon has a similar transport pattern as mineral dust (Fig. 12). As shown in Fig. 12d, the modeled black carbon was found distributed at the western Pacific Ocean. In Fig. 12e, a clear black carbon dome was distributed along 700 hPa, showing a similar pattern as dust. This simulation proposes the consistency of the "double dome" mechanism of Asian dust and biomass burning episodes (Dong et al., 2018; Huang et al., 2019). The issue regarding whether or not such a mechanism could cause the warming effect can be considered as a future study. However, the difference is that the dust dome contains a higher fraction of concentrations as compared to the black carbon dome. Considering the maximum height, the present simulation suggests the dust aerosol can reach up to 500 hPa, which is consistent with Kong et al. (2021). Contrary, the black carbon plume was slightly lower with approximately 600 hPa of the maximum height under the same meteorological condition. As this section essentially discusses the similarity and distinctiveness of natural dust and anthropogenic aerosol at the upper level, we are interested in characterizing the synoptic pattern. Hence, the present simulation did not consider the two-way coupling model, and it is strongly suggested for future study.

4.0 Summary and Conclusions

The chemical transport model is considered sensitive to the dry deposition parameterization besides the dust emission treatment. The present study demonstrates the impact of the four dry deposition parameterizations on aerosol performance in East Asia. It provides a significant analysis of the transboundary transport of East Asian Dust to Taiwan from a case study of 22-31 January 2023. The incorporation of the latest dust emission treatment with PR11 (Pleim and Ran, 2011; Kong et al., 2024) to the CMAQ slightly improved the model performance to -54.05 % from -57.59 %. By implementing the E20 dry deposition scheme, characterized by adding the collection efficiency by interception across the land surface, the CMAQ simulation of the surface PM_{10} has been improved by NMB of -41.9 %, as compared to the dry deposition proposed by S22 (-47.01 %) and P22 (-53.90 %). Moreover, the modeled PM_{10} pattern by CMAQ_Dust_E20 at the upper level (700 hPa) was mostly consistent with the observed PM_{10}, especially in capturing the peak value. The dry deposition of E20 was correlated well with the high altitude in-situ by 0.55, as compared to PR11 (0.47), S22 (0.54) and P22 (0.46). Such a significant difference in PM_{10} improvement has also been shown by modeled $PM_{2.5}$. The simulation of surface $PM_{2.5}$ by PR11 has been improved to -16.53 % from -19.55 %, after using the latest dust treatment, and further enhanced by E20 (-10.65 %), S22 (-15.22 %) and P22 (-8.84 %). Additionally, the simulations of the multiple dust episodes in spring 2021 were re-constructed to evaluate the CMAQ performance over the Asian Continental. The E20 dry deposition scheme outperformed the other schemes with the lowest NMB value in simulating PM_{10} (-25.4 %) and AOD (-26.2%). For the modeled $PM_{2.5}$, S22 performed slightly better than E20, with NMB of -36.29 % and -37.5 %, respectively.

The previous CMAQ model, modulated by Kong et al. (2021; 2024), showed excessive deposition at the marine boundary layer, leading to an underestimation of the modeled surface PM_{10}. However, our updated model, using the E20 and S22 schemes over the entire model domain, has not just reduced, but significantly reduced the 75th percentile of V_d by -50.57 % and -58.27 %, respectively. This precise reduction of V_d of the coarse mode particle, responsible for resolving the PM_{10} simulation underestimation, has not just minimized, but effectively minimized the total loss of aerosol to the surface, leading to a concentration increment. Furthermore, the intense decrease of modeled V_d across the water surface by E20 could play a crucial role in resolving the excessive aerosol deposition over the ocean layer.

In addition, the updated CMAQ was used to investigate the synoptic pattern at the upper level. The transboundary transport of EAD from the Asian Continent towards the western Pacific Ocean at the upper level was associated with the eastward moving trough system. Such transport mechanism is found to bring along the black carbon aerosol, which is primarily the main element of China's human-made emissions. More interestingly, both aerosol profiles created a "long dust-black carbon belt" along the 15°N. The 'double dome mechanism ', a concept proposed by Huang et al. (2019) that depicts the superposition of the two types of aerosol, was also simulated in the present study. However, since the present work did not consider two-way radiative impact, the issue of warming/cooling is proposed in the future study.

Data Availability

MERRA-2 data are available online through the NASA Goddard Earth Sciences Data Information Services Center (GES DISC; https://disc.gsfc.nasa.gov; last access: 01 August 2024). MODIS data used in this study are available at https://asdc.larc.nasa.gov/(last access: 01 August 2024). The observational data at LABS can be ordered by contacting corresponding authors.

Author Contribution

Steven Soon-Kai Kong: Conceptualization; Data curation; Formal analysis; Investigation; Methodology; Software; Validation; Visualization; Writing – original draft; Writing – review and editing.

Joshua S. Fu: Conceptualization; Investigation; Methodology; Formal analysis; Writing – review and editing.

Neng-Huei Lin: Conceptualization; Visualization; Supervision; Funding acquisition; Resources; Writing – review and editing.

Guey-Rong Sheu: Funding acquisition; Resources.

Wei-Syun Huang: Data curation; Software.

Competing Interests

Some authors are members of the editorial board of journal ACP.

Acknowledgments

We acknowledged the National Science and Technology Council of Taiwan, under Project No. NSTC113-2811-M-008-045 for supporting the research. We also acknowledged the staff at LABS, and EPA Taiwan for the provision of the ground-based measurement datasets. We are also thankful to MERRA-2 and MODIS for the satellite product.

References:

Chang, J. and Hanna, S.: Air quality model performance evaluation, Meteorol Atmos Phys., 87, 167–196, https://doi.org/10.1007/s00703-003-0070-7, 2004.

Chuang, M. T, Fu, J. S., Lee, C., Lin, N., Gao, Y., Wang, S., Sheu, G., Hsiao, T., Wang, J., Yen, M., Lin, T., and Thongboonchoo, N.: The Simulation of Long-Range Transport of Biomass Burning Plume and Short-Range Transport of Anthropogenic Pollutants to a Mountain Observatory in East Asia during the 7-SEAS / 2010 Dongsha Experiment, 2933–2949, https://doi.org/10.4209/aaqr.2015.07.0440, 2016.

Chuang, M. T., Fu, J. S., Jang, C. J., Chan, C. C., Ni, P. C., and Lee, C. Te: Simulation of long-range transport aerosols from the Asian Continent to Taiwan by a Southward Asian high-pressure system, Sci. Total Environ., 406, 168–179, https://doi.org/10.1016/j.scitotenv.2008.07.003, 2008.

Chuang, M.-T., Ooi, M. C. G., Lin, N.-H., Fu, J. S., Lee, C.-T., Wang, S.-H., Yen, M.-C., Kong, S. S.-K., and Huang, W.-S.: Study on the impact of three Asian industrial regions on PM2.5 in Taiwan and the process analysis during transport, Atmos. Chem. Phys., 20, 14947–14967, https://doi.org/10.5194/acp-20-14947-2020, 2020.

Dong, X., Fu, J. S., Huang, K., Tong, D., and Zhuang, G.: Model development of dust emission and heterogeneous chemistry within the Community Multiscale Air Quality modeling system and its application over East Asia, Atmos. Chem. Phys., 16, 8157–8180, https://doi.org/10.5194/acp-16-8157-2016, 2016.

Dong, X., Fu, J. S., Huang, K., Lin, N., Wang, S., and Yang, C.: Analysis of the Co-existence of Long-range Transport Biomass Burning and Dust in the Subtropical West Pacific Region, Sci. Rep., 1–10, https://doi.org/10.1038/s41598-018-27129-2, 2018.

Dong, X., Fu, J. S., Huang, K., Zhu, Q., and Tipton, M.: Regional climate effects of biomass burning and dust in East Asia: Evidence from modeling and observation, Geophysical Research Letters, 46. https://doi.org/10.1029/ 2019GL083894, 2019.

Emerson, E. W., Hodshire, A. L., DeBolt, H. M., Bilsback, K. R., Pierce, J. R., McMeeking, G. R., and Farmer, D. K.: Revisiting particle dry deposition and its role in radiative effect estimates, Proc. Natl. Acad. Sci. U. S. A., 117, 26076–26082, https://doi.org/10.1073/pnas.2014761117, 2020.

Foroutan, H., Young, J., Napelenok, S., Ran, L., Appel, K., Gilliam, R., and Pleim, J.: Journal of Advances in Modeling Earth Systems, J. Adv. Model. Earth Syst., 9, 585–606, https://doi.org/10.1002/2013MS000282.Received, 2017.

Gaydos, T. M., Pinder, R., Koo, B., Fahey, K. M., Yarwood, G., and Pandis, S. N.: Development and application of a three-dimensional aerosol chemical transport model, PMCAMx, Atmos. Environ., 41, 2594–2611, https://doi.org/10.1016/j.atmosenv.2006.11.034, 2007.

Gelaro, R., McCarty, W., Suárez, M. J., Todling, R., Molod, A., Takacs, L., Randles, C. A., Darmenov, A., Bosilovich, M. G., Reichle, R., Wargan, K., Coy, L., Cullather, R., Draper, C., Akella, S., Buchard, V., Conaty, A., da Silva, A. M., Gu, W., Kim, G. K., Koster, R., Lucchesi, R., Merkova, D., Nielsen, J. E., Partyka, G., Pawson, S., Putman, W., Rienecker, M., Schubert, S. D., Sienkiewicz, M., and Zhao, B.: The modern-era retrospective analysis for research and applications, version 2 (MERRA-2), J. Clim., 30, 5419–5454, https://doi.org/10.1175/JCLI-D-16-0758.1, 2017.

Giardina, M. and Buffa, P.: A new approach for modeling dry deposition velocity of particles, Atmos. Environ., 180, 11–22, https://doi.org/10.1016/j.atmosenv.2018.02.038, 2018.

Gui, K., Yao, W., Che, H., An, L., Zheng, Y., Li, L., Zhao, H., Zhang, L., Zhong, J., Wang, Y., and Zhang, X.: Record-breaking dust loading during two mega dust storm events over northern China in March 2021: aerosol optical and radiative properties and meteorological drivers, Atmos. Chem. Phys., 22, 7905–7932, https://doi.org/10.5194/acp-22-7905-2022, 2022.

Han, X., Ge, C., Tao, J., Zhang, M., and Zhang, R.: Air quality modeling for a strong dust event in East Asia in March 2010, Aerosol Air Qual. Res., 12, 615–628, https://doi.org/10.4209/aaqr.2011.11.0191, 2012.

He, Y., Yi, F., Yin, Z., Liu, F., Yi, Y., and Zhou, J.: Mega Asian dust event over China on 27–31 March 2021 observed with space-borne instruments and ground-based polarization lidar, Atmos. Environ., 285, 119238, https://doi.org/10.1016/j.atmosenv.2022.119238, 2022.

Hogrefe, C., Bash, J. O., Pleim, J. E., Schwede, D. B., Gilliam, R. C., Foley, K. M., Appel, K. W., and Mathur, R.: An analysis of CMAQ gas-phase dry deposition over North America through grid-scale and land-use-specific diagnostics in the context of AQMEII4, Atmos. Chem. Phys., 23, 8119–8147, https://doi.org/10.5194/acp-23-8119-2023, 2023.

Huang, H.-Y., Wang, S.-H., Huang, W.-X., Lin, N.-H., Chuang, M.-T., da Silva, A. M., Peng, C.-M.: Influence of synoptic-dynamic meteorology on the long-range transport of Indochina biomass burning aerosols, J. Geophys. Res., 111, 125, e2019JD031260. https://doi.org/ 10.1029/2019JD031260, 2020.

Huang, K., Fu, J. S., Lin, N.-H., Wang, S.-H., Dong, X., Wang, G.: Superposition of Gobi Dust and Southeast Asian Biomass Burning: The Effect of Multisource Long - Range Transport on Aerosol Optical Properties and Regional Meteorology Modification, J. Geophys. Res., 124, 16, 9464-9483, https://doi.org/10.1029/2018JD030241, 2019.

Huang, W. S., Griffith, S. M., Lin, Y. C., Chen, Y. C., Lee, C. Te, Chou, C. C. K., Chuang, M. T., Wang, S. H., and Lin, N. H.: Satellite-based emission inventory adjustments improve simulations of long-range transport events, Aerosol Air Qual. Res., 21, 1–16, https://doi.org/10.4209/AAQR.210121, 2021.

Jin, J., Pang, M., Segers, A., Han, W., Fang, L., Li, B., Feng, H., Lin, H. X., and Liao, H.: Inverse modeling of the 2021 spring super dust storms in East Asia, Atmos. Chem. Phys., 22, 6393–6410, https://doi.org/10.5194/acp-22-6393-2022, 2022.

Khan, T. R. and Perlinger, J. A.: Evaluation of five dry particle deposition parameterizations for incorporation into atmospheric transport models, Geosci. Model Dev., 10, 3861–3888, https://doi.org/10.5194/gmd-10-3861-2017, 2017.

Kok, J. F., Parteli, E. J. R., Michaels, T. I., Karam, D. B., and Pierre, U.: The physics of wind-blown sand and dust, 1–119, n.d.

Kong, S. S.-K., Pani, S. K., Griffith, S. M., Ou-Yang, C.-F., Babu, S. R., Chuang, M.-T., Ooi, M. C. G., Huang, W.-S., Sheu, G.-R., and Lin, N.-H.: Distinct transport mechanisms of East Asian dust and the impact on downwind marine and atmospheric environments, Sci. Total Environ., 827, 154255, https://doi.org/10.1016/j.scitotenv.2022.154255, 2022.

Kong, S. S., Fu, J. S., Dong, X., Chuang, M., Chel, M., Ooi, G., Huang, W., Griffith, S. M., Kumar, S., and Lin, N.: Sensitivity analysis of the dust emission treatment in CMAQv5. 2. 1 and its application to long-range transport over East Asia, Atmos. Environ., 118441, https://doi.org/10.1016/j.atmosenv.2021.118441, 2021.

Kong, S. S. K., Ravindra Babu, S., Wang, S. H., Griffith, S. M., Chang, J. H. W., Chuang, M. T., Sheu, G. R., and Lin, N. H.: Expanding the simulation of East Asian super dust storms: physical transport mechanisms impacting the western Pacific, Atmos. Chem. Phys., 24, 1041–1058, https://doi.org/10.5194/acp-24-1041-2024, 2024.

Li, M., Zhang, Q., Kurokawa, J.-I., Woo, J.-H., He, K., Lu, Z., Ohara, T., Song, Y., Streets, D. G., Carmichael, G. R., Cheng, Y., Hong, C., Huo, H., Jiang, X., Kang, S., Liu, F., Su, H., and Zheng, B.: MIX: a mosaic Asian anthropogenic emission inventory under the international collaboration framework of the MICS-Asia and HTAP, Atmos. Chem. Phys., 17, 935–963, https://doi.org/10.5194/acp-17-935-2017, 2017.

Liang, L., Han, Z., Li, J., Xia, X., Sun, Y., Liao, H., Liu, R., and Liang, M.: Science of the Total Environment Emission, transport, deposition, chemical and radiative impacts of mineral dust during severe dust storm periods in March 2021 over East Asia, Sci. Total Environ., 852, 158459, https://doi.org/10.1016/j.scitotenv.2022.158459, 2022.

Liu, S., Xing, J., Sahu, S. K., Liu, X., Liu, S., Jiang, Y., Zhang, H., Li, S., Ding, D., Chang, X., and Wang, S.: Wind-blown dust and its impacts on particulate matter pollution in Northern China: Current and future scenarios, Environ. Res. Lett., 16, 114041, https://doi.org/10.1088/1748-9326/ac31ec, 2021.

Massad, R. S., Nemitz, E., and Sutton, M. A.: Review and parameterisation of bi-directional ammonia exchange between vegetation and the atmosphere, Atmos. Chem. Phys., 10, 10359–10386, https://doi.org/10.5194/acp-10-10359-2010, 2010.

Nemitz, E., Milford, C., and Sutton, M. A.: A two-layer canopy compensation point model for describing bi-directional biosphere-atmosphere exchange of ammonia, Q. J. R. Meteorol. Soc., 127, 815–833, https://doi.org/10.1256/smsqj.57305, 2001.

Ooi, M., Chuang, M.-T., Fu, J., Kong, S., Huang, W.-S., Wang, S.-H., Chan, A., Pani, S., and Lin, N.-H.: Improving prediction of trans-boundary biomass burning plume dispersion: from northern peninsular Southeast Asia to downwind western north Pacific Ocean, Atmos. Chem. Phys., 20, 14947–14967, https://doi.org/10.5194/acp-2020-1283, 2021.

Pani, S. K., Wang, S. H., Lin, N. H., Lee, C. Te, Tsay, S. C., Holben, B. N., Janjai, S., Hsiao, T. C., Chuang, M. T., and Chantara, S.: Radiative effect of springtime biomass-burning aerosols over northern indochina during 7-SEAS/BASELInE 2013 campaign, Aerosol Air Qual. Res., 16, 2802–2817, https://doi.org/10.4209/aaqr.2016.03.0130, 2016.

Pani, S. K., Wang, S. H., Lin, N. H., Chantara, S., Lee, C. Te, and Thepnuan, D.: Black carbon over an urban atmosphere in northern peninsular Southeast Asia: Characteristics, source apportionment, and associated health risks, Environ. Pollut., 259, 113871, https://doi.org/10.1016/j.envpol.2019.113871, 2020.

Ramanthan, V and Carmicheal, G.: Climate change due to BC, Nat. Geosci., 1, 221–227, 2008.

Ravindra Babu, S., Ou-Yang, C. F., Griffith, S. M., Pani, S. K., Kong, S. S. K., and Lin, N. H.: Transport pathways of carbon monoxide from Indonesian fire pollution to a subtropical high-Altitude mountain site in the western North Pacific, Atmos. Chem. Phys., 23, 4727–4740, https://doi.org/10.5194/acp-23-4727-2023, 2023.

Ryu, Y. H. and Min, S. K.: Improving Wet and Dry Deposition of Aerosols in WRF-Chem: Updates to Below-Cloud Scavenging and Coarse-Particle Dry Deposition, J. Adv. Model. Earth Syst., 14, https://doi.org/10.1029/2021MS002792, 2022.

Saylor, R. D., Baker, B. D., Lee, P., Tong, D., Pan, L., and Hicks, B. B.: The particle dry deposition component of total deposition from air quality models: right, wrong or uncertain?, Tellus, Ser. B Chem. Phys. Meteorol., 71, 1–22, https://doi.org/10.1080/16000889.2018.1550324, 2019.

Shu, Q., Koo, B., Yarwood, G., and Henderson, B. H.: Strong influence of deposition and vertical mixing on secondary organic aerosol concentrations in CMAQ and CAMx, Atmos. Environ., 171, 317–329, https://doi.org/10.1016/j.atmosenv.2017.10.035, 2017.

Slinn, W. G. N.: Predictions for particle deposition to vegetative canopies, Atmos. Environ., 16, 1785–1794, https://doi.org/10.1016/0004-6981(82)90271-2, 1982.

Tang, W., Dai, T., Cheng, Y., Wang, S., and Liu, Y.: A Study of a Severe Spring Dust Event in 2021 over East Asia with WRF-Chem and Multiple Platforms of Observations, Remote Sens., 14, 3795, https://doi.org/10.3390/rs14153795, 2022.

Wang, W., Zhou, H., Lyu, R., Shao, L., Li, W., Xing, J., Zhao, Z., Li, X., Zhou, X., and Zhang, D.: Organic Carbon and Elemental Carbon in Two Dust Plumes at a Coastal City in North China, Aerosol Air Qual. Res., 24, https://doi.org/10.4209/aaqr.240002, 2024.

Wesley, M. L.: Parameterization of Surface Resistances to Gaseous Dry Deposition in Regional-Scale Numerical Models, Atmos. Environ., 23, 1293–1304, 1989.

Xiao, H. W., Xu, Y., and Xiao, H. Y.: Source apportionment of black carbon aerosols in winter across China, Atmos. Environ., 298, https://doi.org/10.1016/j.atmosenv.2023.119622, 2023.

Zeng, Y., Wang, M., Zhao, C., Chen, S., Liu, Z., Huang, X., and Gao, Y.: WRF-Chem v3.9 simulations of the East Asian dust storm in May 2017: Modeling sensitivities to dust emission and dry deposition schemes, Geosci. Model Dev., 13, 2125–2147, https://doi.org/10.5194/gmd-13-2125-2020, 2020.

Zhang, L., Gong, S., Padro, J., and Barrie, L.: A size-segregated particle dry deposition scheme for an atmospheric aerosol module, Atmos. Environ., 35, 549–560, https://doi.org/10.1016/S1352-2310(00)00326-5, 2001.

Zheng, B., Tong, D., Li, M., Liu, F., Hong, C., Geng, G., Li, H., Li, X., Peng, L., Qi, J., Yan, L., Zhang, Y., Zhao, H., Zheng, Y., He, K., and Zhang, Q.: Trends in China's anthropogenic emissions since 2010 as the consequence of clean air actions, Atmos. Chem. Phys., 18, 14095–14111, https://doi.org/10.5194/acp-18-14095-2018, 2018.

Table 1. Model settings.

Model setting	Descriptions
Period	12 March-20 April 2021 and 22-31 January 2023
Domain	d01, d02, and d03 with 45 KM, 15 KM, and 5 KM of the resolutions, respectively
Boundary condition	NCEP FNL lateral boundary condition
Surface and land surface model	NOAH
Numerical weather model	WRF v40, including grid and observation nudging at d01.
Chemical transport model	CMAQ v5.4
Gas-phase chemistry and aerosol mechanism	CB06e51 + AE7
Emission Inventory	MICS-ASIA III emission in 2023, adjusted from the emission in 2017 (Zhang et al., 2018) based on the OMI-NO_x satellite (Huang et al., 2021).
Online dust treatment	The windblown dust treatment suggested by Kong et al. (2024).
Dry deposition option	M3DRY (PR11) and STAGE (E20, S22 and P22).

Table 2. Simulation scenarios used in this present study.

Scenarios	Descriptions
CMAQ_Off_PR11	Without in-line dust calculation, with the M3DRY dry deposition algorithm by Pleim and Ran (2011).
CMAQ_Dust_PR11	Implement the latest refined dust treatment proposed by Kong et al. (2024), with the M3DRY dry deposition algorithm by Pleim and Ran (2011).
CMAQ_Dust_E20	Same as CMAQ_Dust_PR11, but with the STAGE dry deposition algorithm by Emerson et al. (2020).
CMAQ_Dust_S22	Same as CMAQ_Dust_PR11, but with the STAGE dry deposition algorithm by Shu et al. (2022).
CMAQ_Dust_P22	Same as CMAQ_Dust_PR11, but with the STAGE dry deposition algorithm by Pleim et al. (2022).

Table 3. Statistical evaluation for PM_{10} and $PM_{2.5}$ concentrations during 22-31 January 2023 for Cape Fuguei under the multiple simulation scenarios.

	Benchmark	CMAQ-M3DRY		CMAQ-STAGE		
		Off _PR11	Dust_PR11	Dust_E20	Dust_S22	Dust_P22
			PM_{10}			
MeanObs		49.97	49.97	49.97	49.97	49.97
MeanMod		21.19	22.97	29.04	26.48	23.04
NMSE		0.82	0.71	0.49	0.56	0.71
NMB	± 85%	-57.59	-54.05	-41.90	-47.01	-53.90
R	> 0.35	0.41	0.44	0.52	0.46	0.42
NMBF		-1.36	-1.18	-0.72	-0.89	-1.17
			$PM_{2.5}$			
MeanObs		15.52	15.52	15.52	15.52	15.52
MeanMod		12.48	12.95	13.86	14.15	13.16
NMSE		0.31	0.29	0.29	0.30	0.31
NMB	± 85%	-19.55	-16.53	-10.65	-8.84	-15.22
R	> 0.35	0.52	0.55	0.53	0.53	0.52
NMBF		-0.24	-0.20	-0.12	-0.10	-0.18

Note: the definition of the statistical formulas NMSE: Normalized Mean Square Error; NMB: Normalized Mean Bias; R: Correlation Coefficient and NMBF: Normalized Mean Bias Factor

Table 4. CMAQ evaluation for PM_{10} and $PM_{2.5}$ against the averaged 100 observation sites across mainland China (Fig. S1) and AOD against MODIS daily observation near the dust source region (above 30°N) with Normalized Mean Bias (NMB) under the multiple simulation scenarios (Fig. S3). Spring 2021, 3.15, 3.27, and 4.18 represent the evaluation period by 12 March-20 April 2021, 14-16 March 2021, 26-28 March 2021, and 17-19 April 2021, respectively.

Parameters	Period	CMAQ-M3DRY		CMAQ-STAGE		
		Off_PR11	Dust_PR11	Dust_E20	Dust_S22	Dust_P22
PM_{10}	Spring 2021	-79.15	-60.53	-25.43	-45.97	-59.82
$PM_{2.5}$	Spring 2021	-60.94	-44.84	-37.50	-36.29	-42.47
AOD	3.15	-81.92	-49.54	-38.97	-46.41	-48.45
	3.27	-75.10	-46.12	-36.39	-41.84	-44.52
	4.18	-55.88	-16.49	-3.20	-7.83	-14.52
	Mean AOD	-70.97	-37.38	-26.19	-32.03	-35.83

Table 5. Average deposition velocity and the percentage change by PR11 corresponding to E20, S22, and P22, for Aitken, Accumulation, and Coarse modes over land and ocean boundary layer, respectively.

Dry deposition schemes	Aitken		Accumulation		Coarse	
	Land	Ocean	Land	Ocean	Land	Ocean
PR11 ($cm\ s^{-1}$)	0.080	0.062	0.061	0.042	0.264	0.109
E20 ($cm\ s^{-1}$)	0.090	0.074	0.065	0.040	0.139	0.060
S22 ($cm\ s^{-1}$)	0.219	0.117	0.120	0.064	0.078	0.085
P22 ($cm\ s^{-1}$)	0.085	0.062	0.072	0.043	0.290	0.116
ΔE20 (%)	12.66	20.06	5.43	-5.19	-47.10	-44.65
ΔS22 (%)	173.74	89.45	96.52	52.35	-70.29	-21.44
ΔP22 (%)	6.10	1.37	17.66	1.52	10.06	6.86

Note: the Δ represents the percentage change by PR11 relative to E20, S22, and P22.

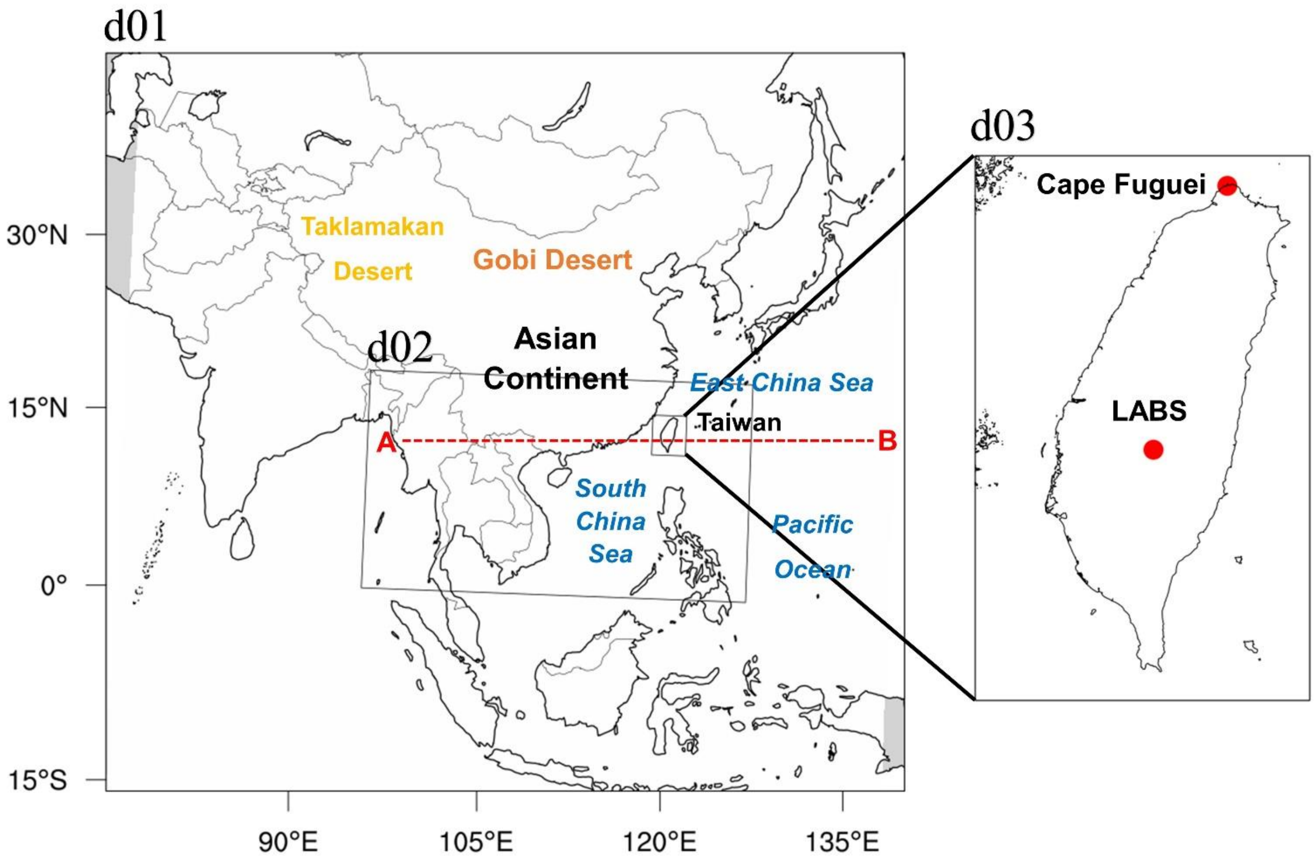

Figure 1: Modeling domain configuration in East Asia. Ground-based air quality stations in Taiwan at Cape Fuguei and Lulin Atmospheric Background Station (LABS) are shown in the zoomed panel. The red dash line (A→B) represents the transects that the aerosol plumes traveled along in this study and that are discussed in Section 3.4;

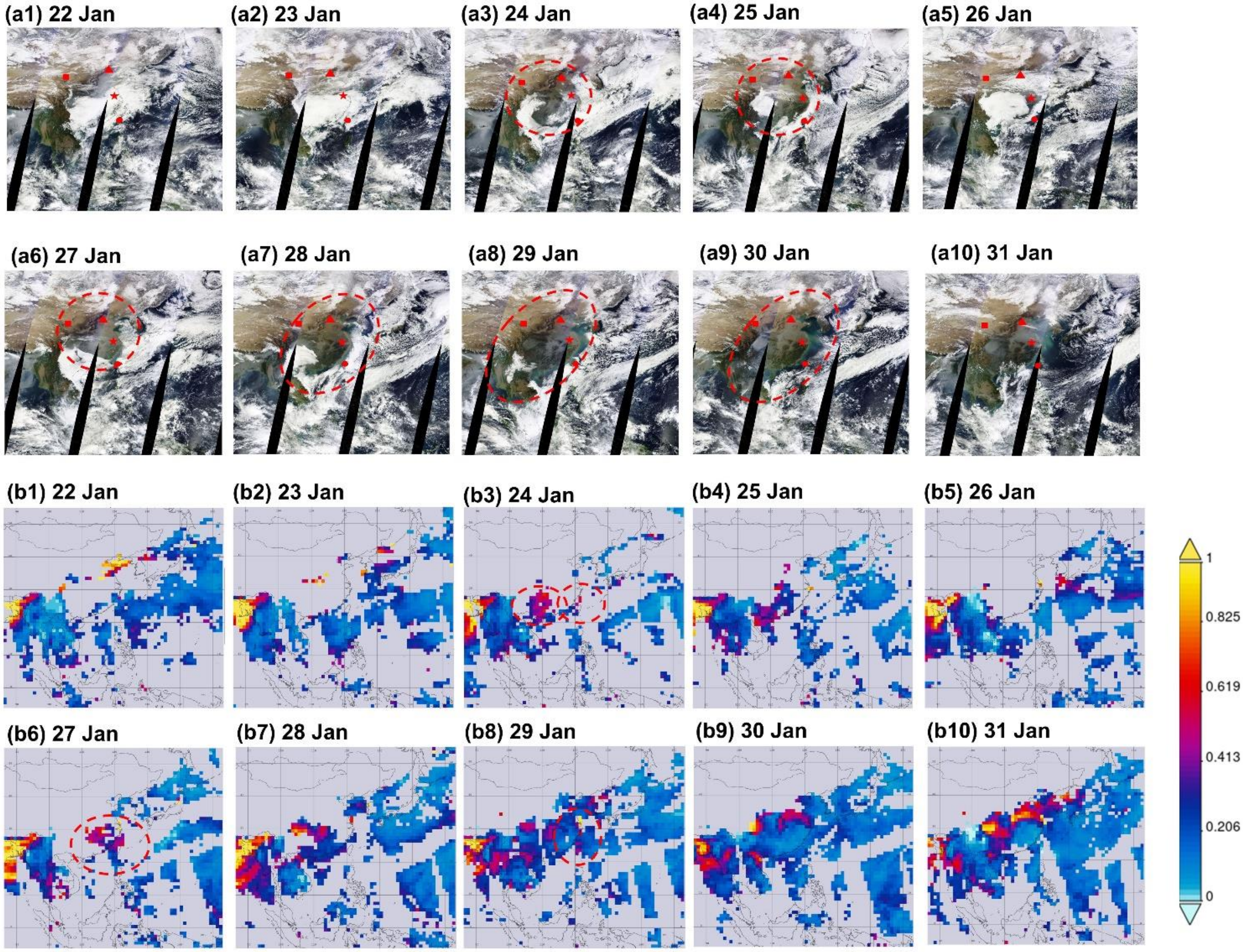

Figure 2: MODIS Terra images (a1-a10) and MODIS aerosol optical depth AOD at 550 nm (b1-b10) showing dust outbreak across East Asia during 22-31 January 2023. Red Rectangular, triangle, star and circle indicate Lanzhou, Beijing, Shanghai and Taiwan. The red circle with dash line indicates the dust plume.

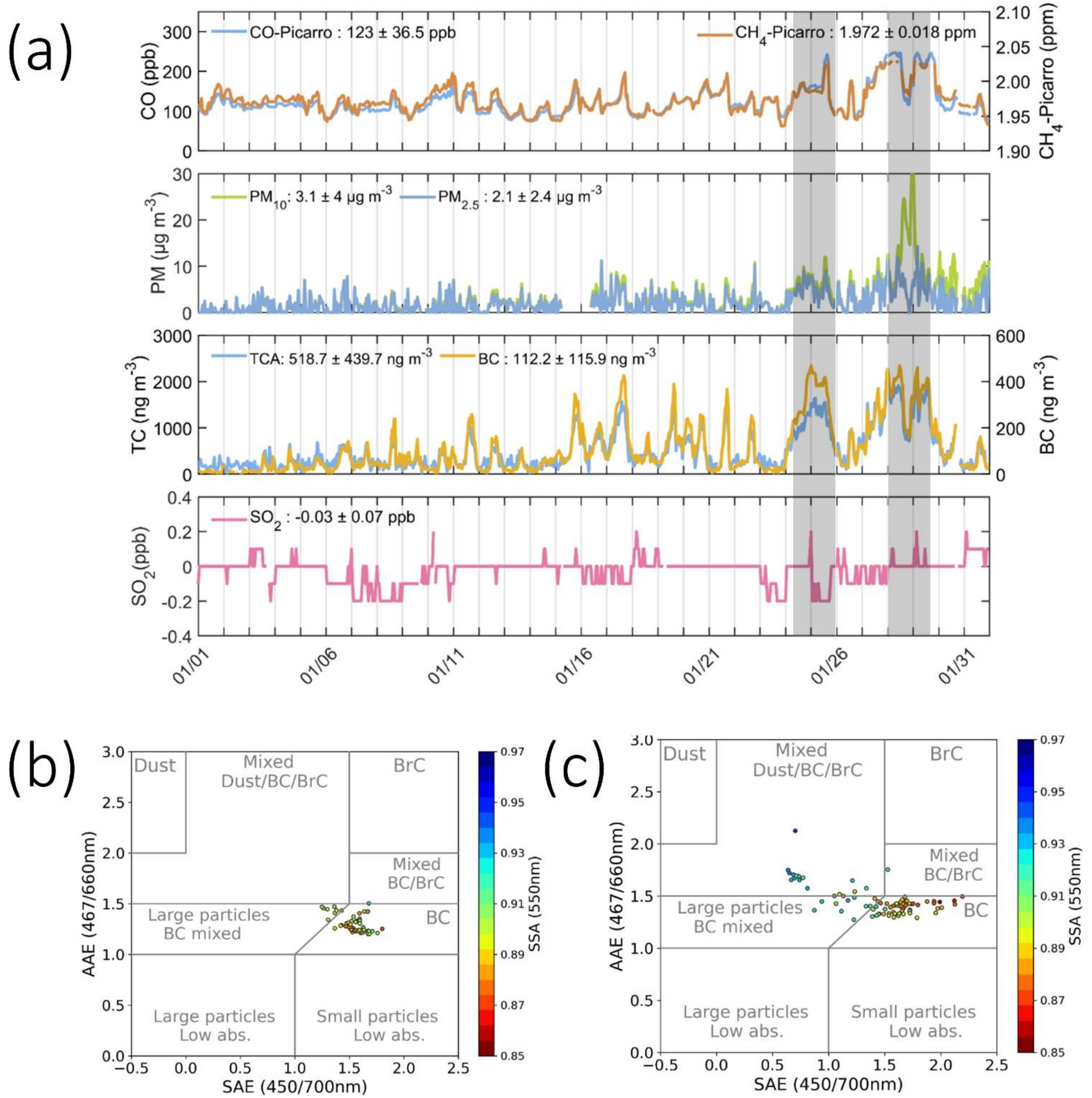

Figure 3: (a) Time series of observed pollutants over LABS during January 2023. The aerosol radiation properties during (b) 24-26 January and (c) 27-30 January 2023.

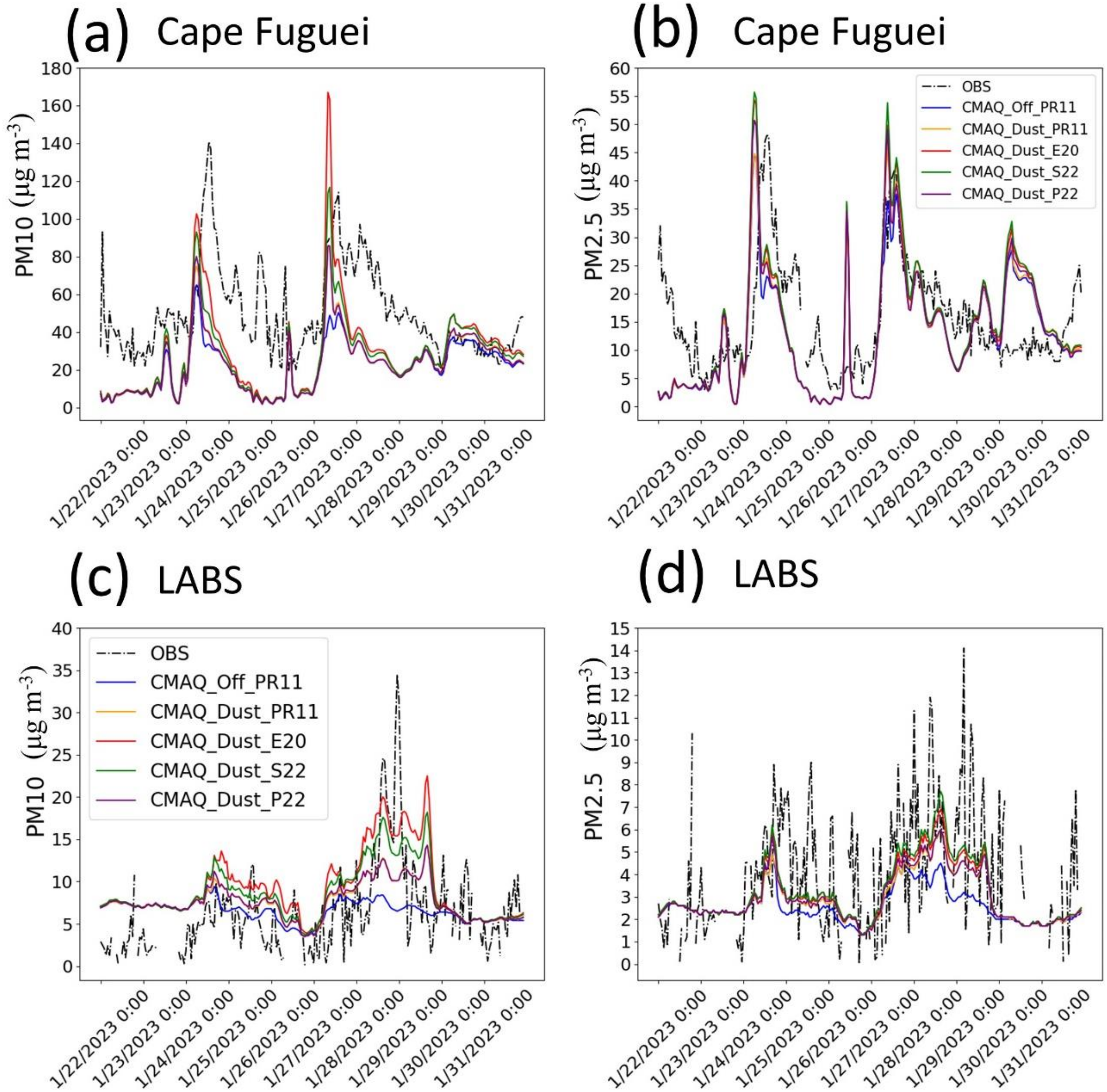

Figure 4: Time series of PM_{10} (left panel) and $PM_{2.5}$ (right panel) concentrations during 22-31 January 2023 under multiple deposition schemes over the Cape Fuguei (upper panel) and LABS (lower panel), representing the surface and high altitude, respectively.

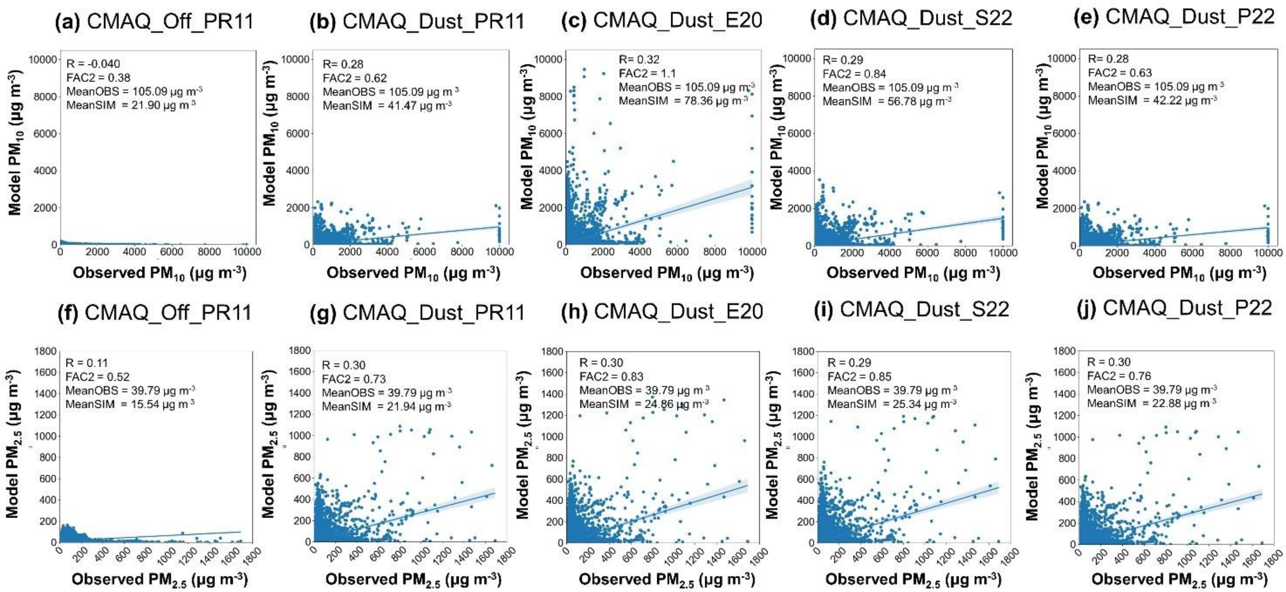

Figure 5: The scatter plot of the observed against modeled PM_{10} (a-e) and $PM_{2.5}$ (f-j) for CMAQ_Off_PR11 (a, f), CMAQ_Dust_PR11 (b, g), CMAQ_Dust_E20 (c, h), CMAQ_Dust_S22 (d, I and CMAQ_Dust_P22 (e, j), at the 100 sites of the mainland China on 12 March-20 April 2021 (http://www.aqistudy.cn/). R is the correlation coefficient between the observation and model; FAC2 is the factor of two; MeanOBS and MeanSIM are the mean of PM from observation and model, respectively.

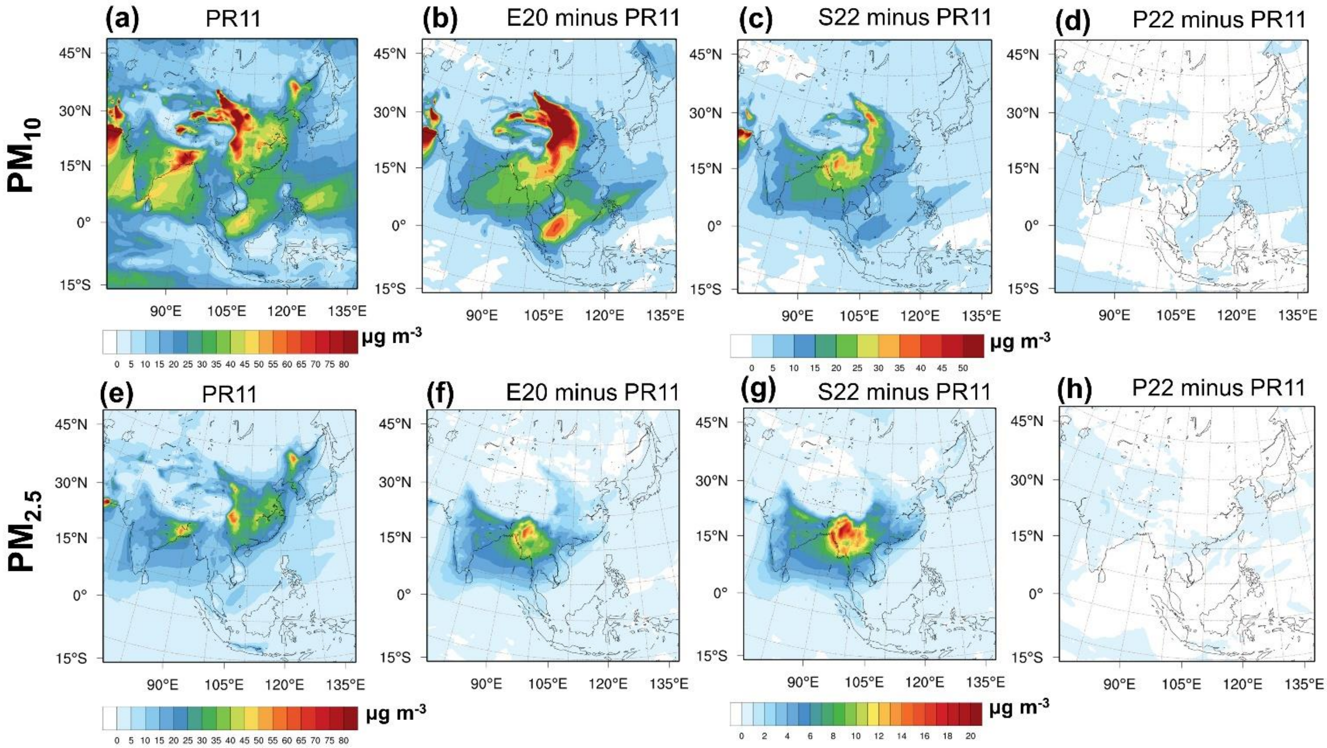

Figure 6: CMAQ estimated 10 days (22-31 January 2023) averaged mean (a-d) PM_{10} and (e-h) $PM_{2.5}$ for (a, e) PR11 dry deposition scheme and the corresponding concentration changes using (b, f) E20, (c, g) S22 and (d, h) P22 schemes.

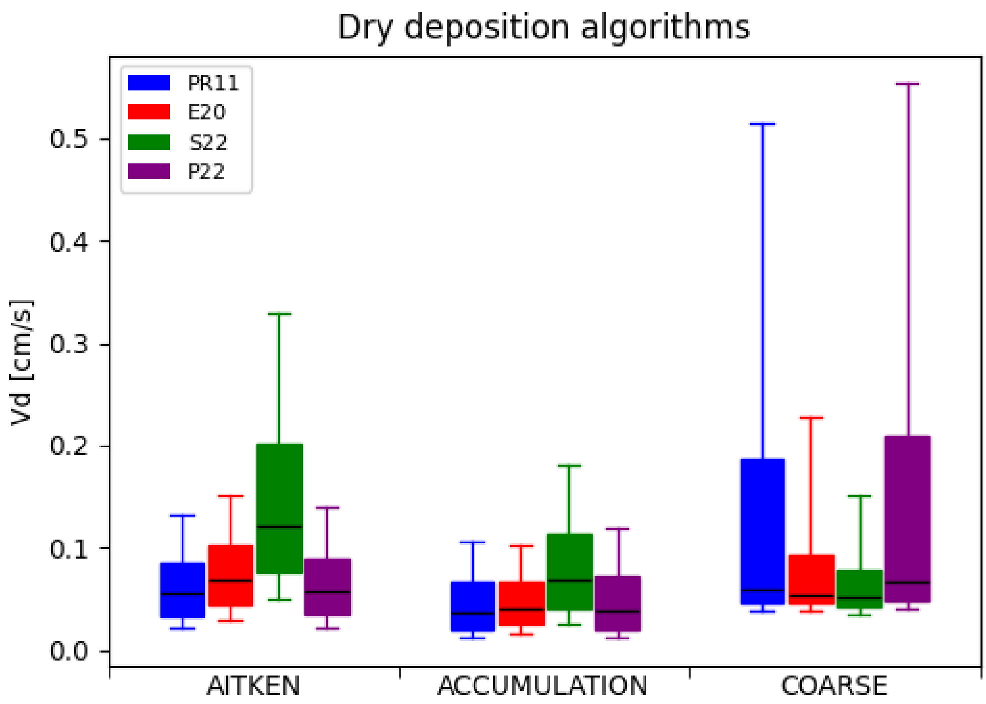

Figure 7: 10-days averaged dry V_d predicted by CMAQv5.4 for the Aitken, accumulation, and coarse particle modes using the PR11(blue), E20(red), S22(green) and P22(purple) particle dry deposition schemes. The variability illustrated by the boxes and whiskers corresponds to spatial variability in annually averaged values throughout the CMAQ domain.

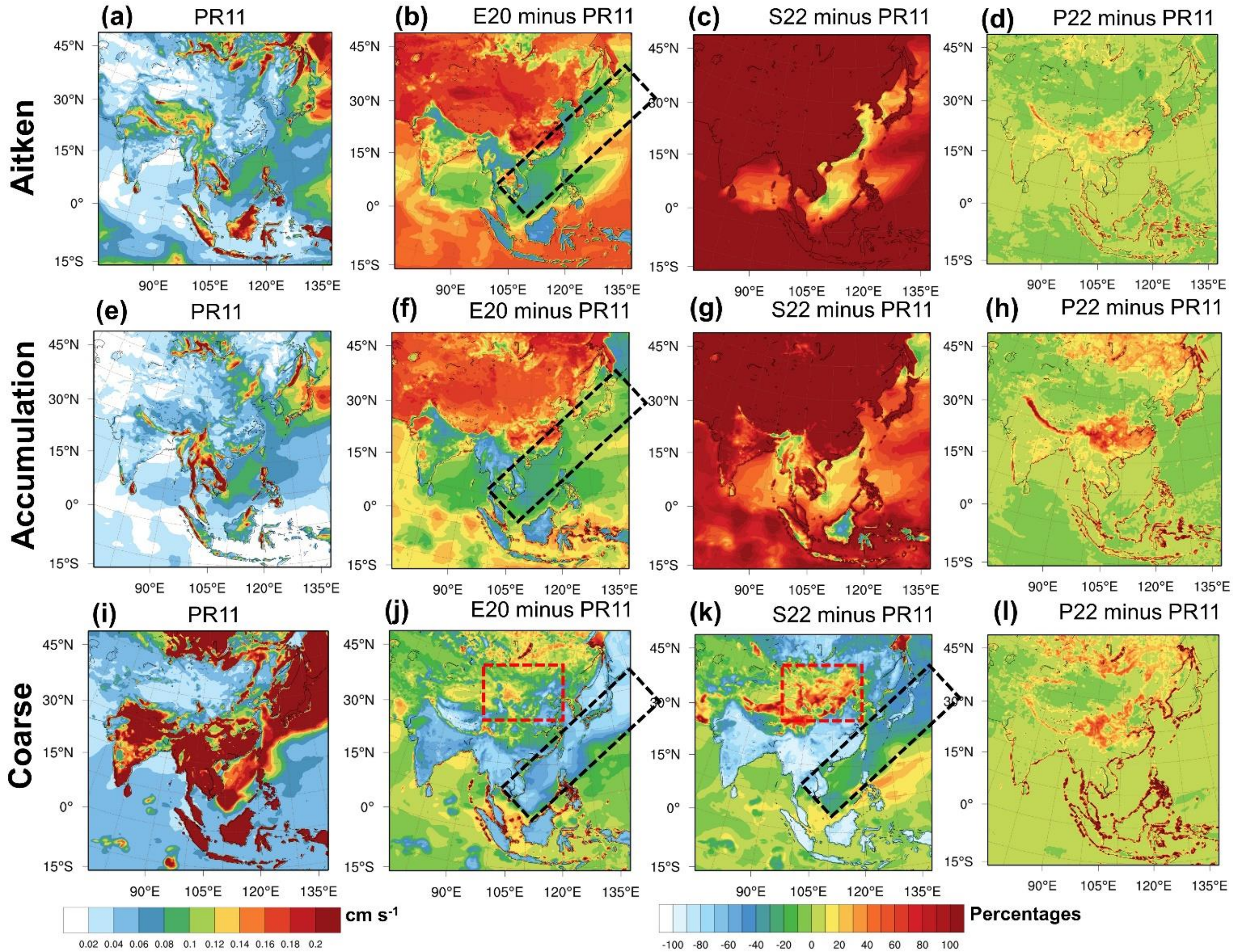

Figure 8: CMAQ estimated 10 days (22-31 January 2023) averaged for the (a-d) Aitken, (e-h) accumulation, and (i-l) coarse particle modes for PR11 dry deposition scheme (a, e, i) and the corresponding concentration percentage changes (%) using (b, f, j) E20, (c, g, k) S22 and (d, h, l) P22 schemes. Red-dash rectangular indicates the region across northwest China; Black-dash rectangular indicates the marine boundary layer.

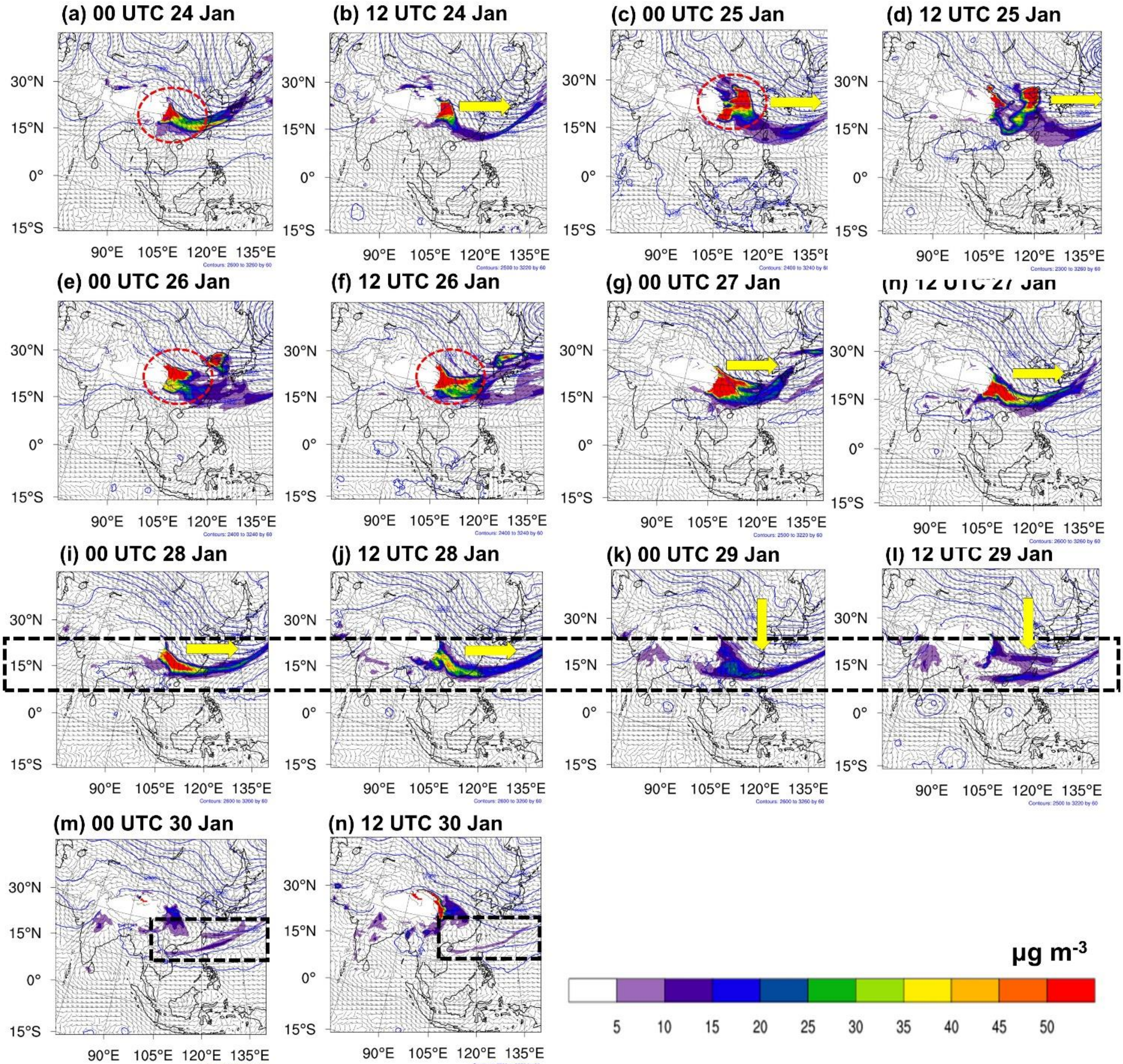

Figure 9: CMAQ mineral dust aerosol concentration at the 700 hPa during 24-30 January 2023. The yellow arrows highlight the trough moving direction. The dash-black rectangular box highlights the dust belt.

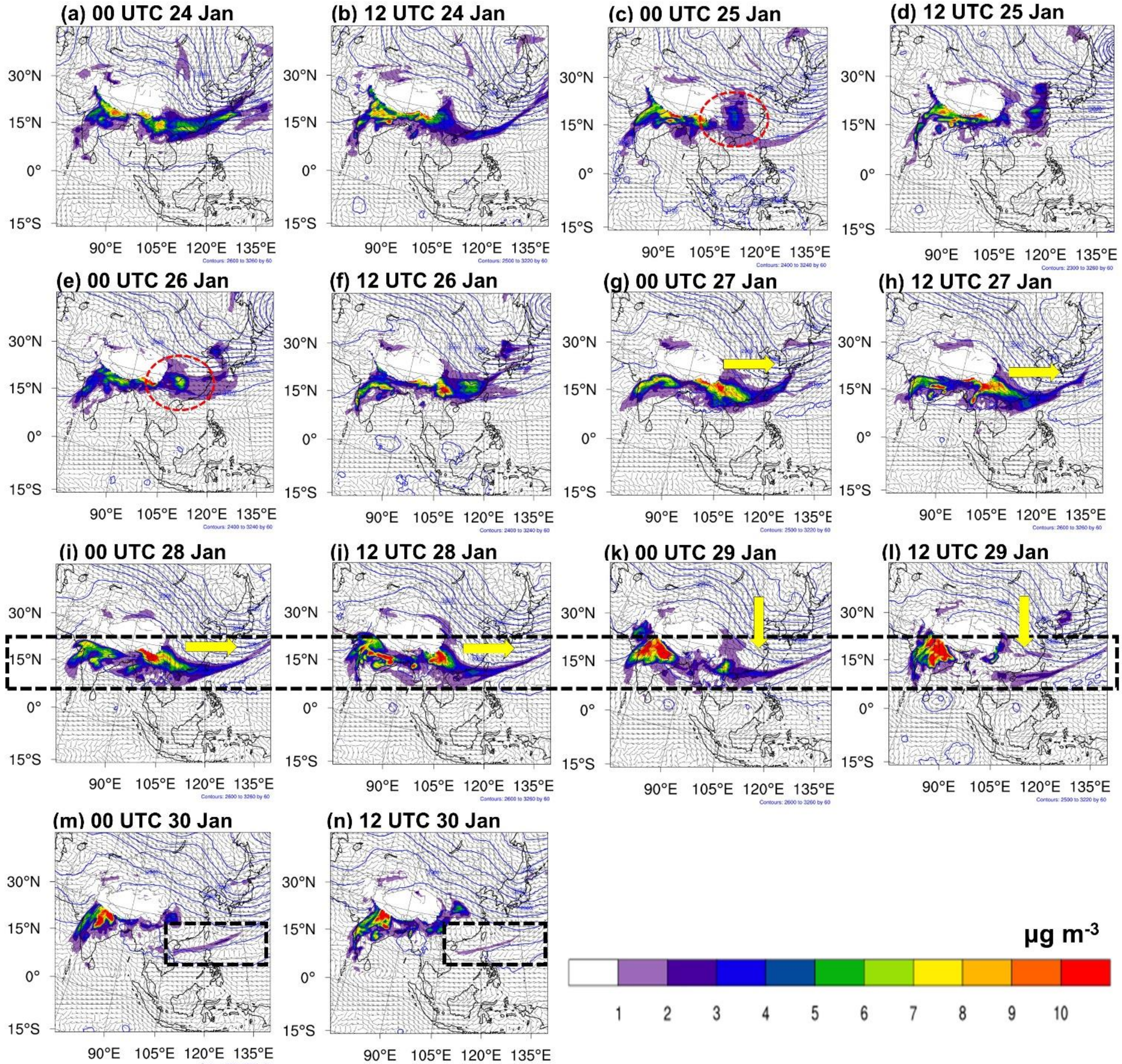

Figure 10: CMAQ black carbon concentration at the 700 hPa during 24-30 January 2023. The yellow arrows highlight the trough moving direction. The dash-black rectangular box highlights the dust belt.

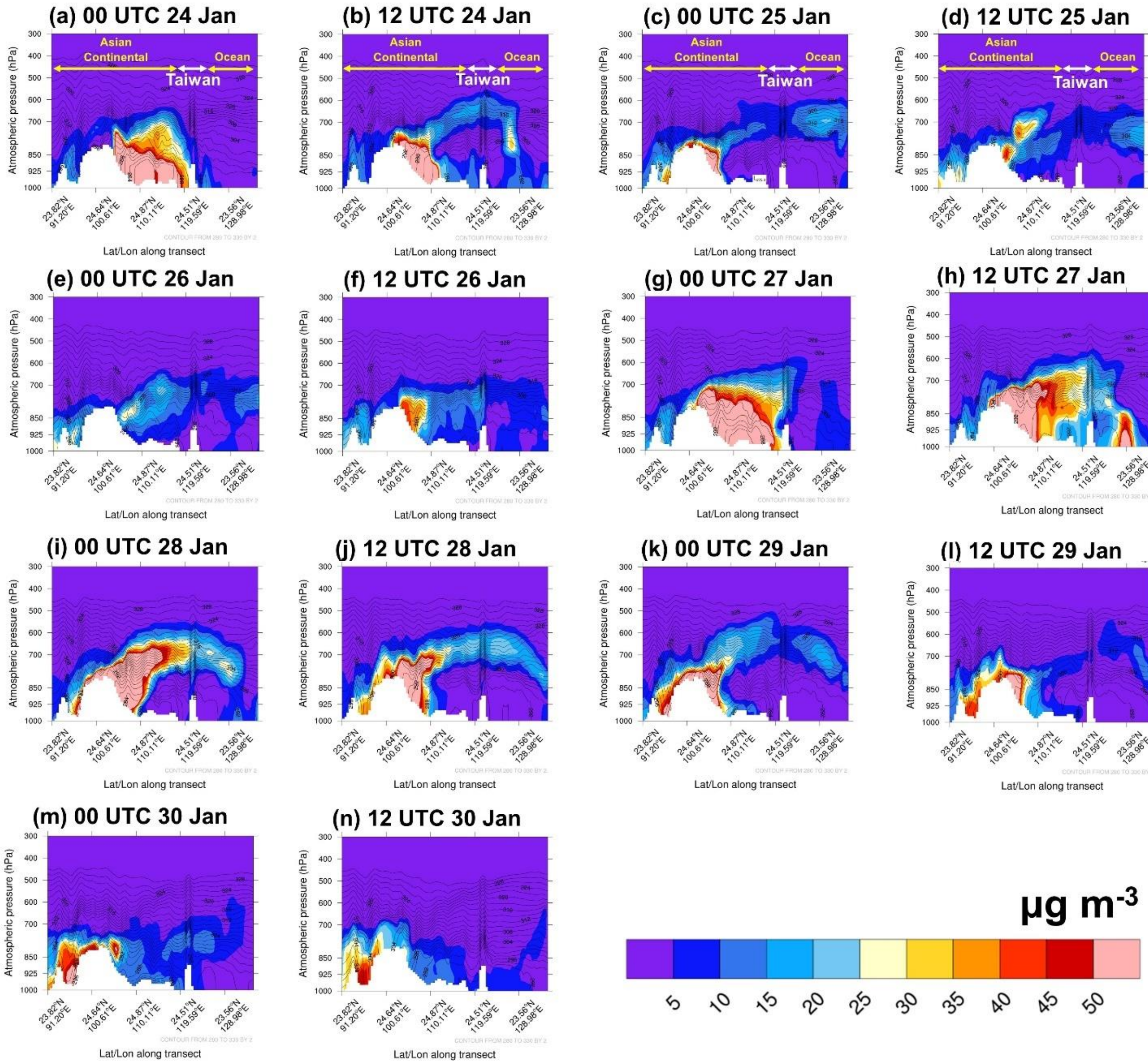

Figure 11: Vertical profile of simulated dust aerosol for the CMAQ simulation during 24-30 January 2023.

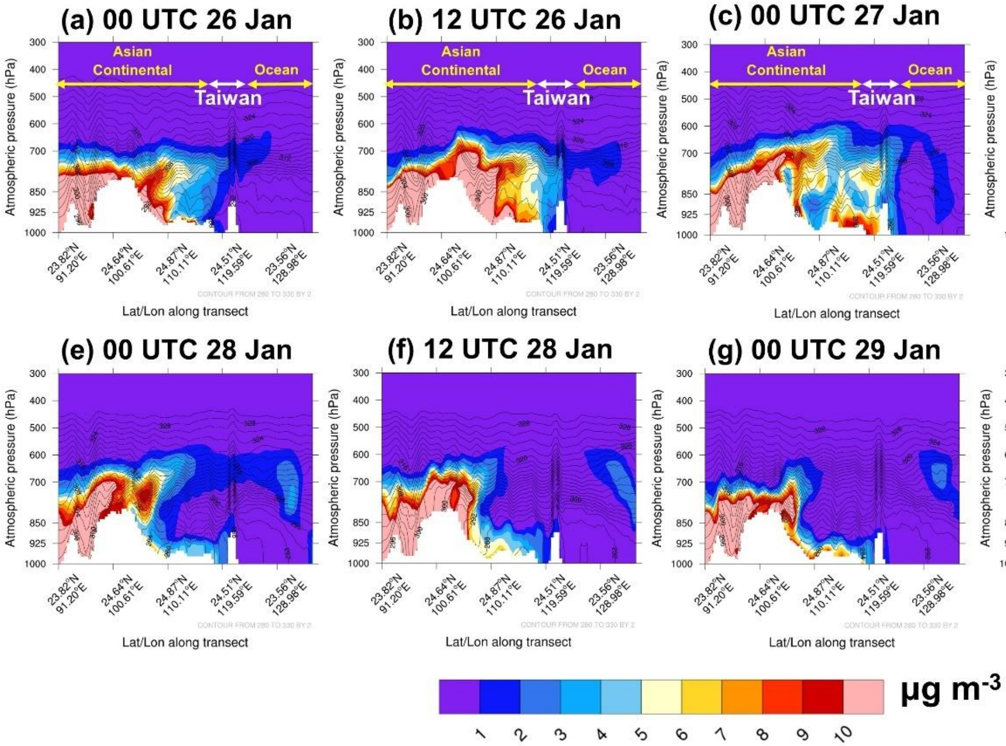

Figure 12: Vertical profile of simulated black carbon aerosol for the CMAQ simulation during 26-29 January 2023.